Complex Distribution of Diphosphate Groups in the Structure of V(IV) Phosphates $A(VO)_3(P_2O_7)_2$ (A = Sr, Pb, and Ba)

M. M. Borel, M. Hervieu, A. Leclaire, C. Michel, J. Chardon, J. Provost, and B. Raveau

Laboratoire CRISMAT, UMR 6508 associée au CNRS, ISMRA et Université de Caen,
6 Boulevard du Maréchal Juin, 14050 CAEN Cedex, France

Received July 29, 1999

New V(IV) diphosphates $A(VO)_3(P_2O_7)_2$ have been synthesized for A = Ba, Sr, and Pb. Their X-ray diffraction and electron microscopy studies show their complex crystal chemistry. The polycrystalline samples of the Ba, Sr, and Pb phases and the single crystals of Sr and Pb phases exhibit a $P2_12_12_1$-type structure (called α form) similar to that observed for $K(VO)_3(P_2O_7)_2$. For a single crystal of $Ba(VO)_3(P_2O_7)_2$, a new structural form, called β, has been stabilized. It crystallizes in the $P11b$ space group, with cell parameters similar to those of the α form. This structure, closely related to that of the α form, differs from the latter by the distribution of the barium cations and the surrounding P_2O_7 groups. The HREM study of polycrystalline β-$Ba(VO)_3(P_2O_7)_2$ shows the great flexibility of this structure. It demonstrates the coexistence of the two structures, $P2_12_12_1$ and $P11b$, in many crystallites, in the form of $P11b$ intergrowth defects in the $P2_12_12_1$ matrix.

Introduction

Vanadium phosphates have been extensively explored with a view to applications for catalysis.[1] Among the various original structures of the V(IV) phosphates[2−16] and of the mixed valent V(IV)−V(V) phosphates,[17−19] that of the diphosphate $K(VO)_3(P_2O_7)_2$[19] is of interest. It exhibits close relationships indeed with the diphosphate tungsten bronzes with hexagonal tunnels,[20] actually investigated for their charge density wave properties.[21] A similar intersecting tunnel structure should be expected by substituting barium for potassium, so that tetravalent vanadium would be obtained instead of the mixed valence V(IV)−V(V) for $K(VO)_3(P_2O_7)_2$. In the present paper, mainly devoted to the synthesis, crystal growth, and structural study of $Ba(VO)_3(P_2O_7)_2$, we show that there exist two forms of this phase, which both belong to the $K(VO)_3(P_2O_7)_2$-type but differ by the distribution of the P_2O_7 groups in the structure. We also demonstrate the possibility of synthesizing and growing single crystals of isotypic phases for strontium and lead.

Structural and Magnetic Characterization. The X-ray powder diffraction (XRPD) patterns were registered by step scanning in the range $8° \leq 2\theta \leq 80°$ with a vertical Philips diffractometer, using Cu Kα radiation.

The intensity data of single crystals were collected on an Enraf Nonius four-circle diffractometer using Mo Kα radiation. The cell parameters were determined by diffractometric techniques at 294 K with a least-squares refinement based upon 25 reflections in the range $18° < \theta < 22°$. The reflections were corrected for the Lorentz and polarization effects, as well as for absorption (Gaussian method).

The electron diffraction (ED) study was carried out with a JEOL 200 CX electron microscope fitted with an eucentric goniometer (±60°), and the high-resolution electron microscopy (HREM) study was carried out with a TOPCON 002B microscope (200 kV and $C_s = 0.4$ mm). Both microscopes are equipped with KEVEX energy-

---

(1) Hodnett, B. L. *Catal. Rev. Sci. Eng.* **1985**, *27*, 373.
(2) Gorbunova, Y. U.; Linde, S. A.; Lavrova, V.; Tananaev, I. V. *Dokl. Akad. Nauk SSSR* **1980**, *250*, 350.
(3) Leclaire, A.; Chahboun, H.; Groult, D.; Raveau, B. *J. Solid State Chem.* **1988**, *77*, 170.
(4) Lii, K. H.; Wang, S. L. *J. Solid State Chem.* **1989**, *82*, 239.
(5) Lii, K. H.; Tsai, H. J.; Wang, S. L. *J. Solid State Chem.* **1990**, *87*, 396.
(6) Lii, K. H.; Tsai, H. J. *J. Solid State Chem.* **1991**, *90*, 291.
(7) Benhamada, L.; Grandin, A.; Borel, M. M.; Leclaire, A.; Leblanc, M.; Raveau, B. *J. Solid State Chem.* **1992**, *101*, 154.
(8) Kang, H. Y.; Lee, W. C.; Wang, S. L. *Inorg. Chem.* **1992**, *31*, 4743.
(9) Lii, K. H.; Chueh, R. R.; Kang, H. Y.; Wang, S. L. *J. Solid State Chem.* **1992**, *99*, 72.
(10) Grandin, A.; Chardon, J.; Borel, M. M.; Leclaire, A.; Raveau, B. *J. Solid State Chem.* **1992**, *99*, 297.
(11) Grandin, A.; Chardon, J.; Borel, M. M.; Leclaire, A.; Raveau, B. *J. Solid State Chem.* **1992**, *C48*, 1913.
(12) Lii, K. H.; Liu, W. C. *J. Solid State Chem.* **1993**, *103*, 138.
(13) Harrison, W.; Lim, E.; Vaughey, J. T.; Jacobson, A.; Goshorn, D.; Johnson, J. *J. Solid State Chem.* **1995**, *116*, 77.
(14) Borel, M. M.; Leclaire, A.; Chardon, J.; Provost, J.; Rebbah, H.; Raveau, B. *J. Solid State Chem.* **1997**, *132*, 41.
(15) Daidouh A.; Veiga M. L.; Pico C. *J. Solid State Chem.* **1997**, *130*, 28.
(16) Berrah, F.; Leclaire, A.; Borel, M. M.; Guesdon, A.; Raveau, B. *Acta Cryst.* **1999**, *C55*, 288.
(17) Grandin, A.; Chardon, J.; Borel, M. M.; Leclaire, A.; Raveau, B. *J. Solid State Chem.* **1993**, *104*, 226.
(18) Borel, M. M.; Leclaire, A.; Chardon, J.; Michel, C.; Provost, J.; Raveau, B. *J. Solid State Chem.* **1998**, *135*, 329.
(19) Benhamada, L.; Grandin, A.; Borel, M. M.; Leclaire, A.; Raveau, B. *J. Solid State Chem.* **1992**, *97*, 131.
(20) Labbe, P. H.; Goreaud, M.; Raveau, B. *J. Solid State Chem.* **1983**, *50*, 163.
(21) Schlenker, C.; Dumas, J.; Greenblatt, M.; van Smaalen, S. *Physics and Chemistry of Low Dimensional Inorganic Condutors*; NATO ASI Series; Plenum: New York, 1996.

10.1021/cm9904842 CCC: $18.00

Table 1. Summary of Crystal Data, Intensity Measurements, and Structure Refinement Parameters for α-$Sr(VO)_3(P_2O_7)_2$, α-$Pb(VO)_3(P_2O_7)_2$, and β-$Ba(VO)_3(P_2O_7)_2$

	Sr	Pb	Ba	
		1. Crystal Data:		
cell dimensions	$a = 7.594(1)$ Å	$a = 7.600(1)$ Å	$a = 7.6871(8)$ Å	α = 90°
	$b = 10.075(1)$ Å	$b = 10.0883(9)$ Å	$b = 10.0898(7)$ Å	$\beta = 90°$
	$c = 16.291(1)$ Å	$c = 16.332(2)$ Å	$c = 16.746(3)$ Å	$\gamma = 90.036(7)°$
volume	$V = 1246.4(3)$ Å^3	$V = 1252.2(3)$ Å^3	$V = 1298.8(3)$ Å^3	
space group	$P2_12_12_1$	$P2_12_12_1$	$P11b$	
Z	4	4	4	
		2. Data Collection:		
λ (Mo Kα)	0.710 73 Å	0.710 73 Å	0.710 73 Å	
scan mode	$\omega - {}^2/_3\theta$	$\omega - {}^4/_3\theta$	$\omega - {}^2/_3\theta$	
scan width (°)	$1 + 0.35 \tan \theta$	$1 + 0.35 \tan \theta$	$1 + 0.35 \tan \theta$	
slit aperture (mm)	$1 + \tan \theta$	$1 + \tan \theta$	$1 + \tan \theta$	
maximum θ (°)	45	45	45	
standard reflections		three measured every hour		
measured reflections	11091	11474	11318	
reflections with $I > 3\sigma(I)$	2920	3428	3700	
μ (mm^{-1})	7.06	16.19	5.68	
		3. Refinement:		
parameters refined	129	228	233	
agreement factors	$R = 0.040$	$R = 0.026$	$R = 0.057$	
	$R_w = 0.037$	$R_w = 0.023$	$R_w = 0.042$	
weighting scheme	$w = 1/\sigma(F)^2$	$w = 1/\sigma(F)^2$	$w = 1/\sigma(F)^2$	
Δ/σ_{max}	0.007	0.003	0.7	
$\Delta\rho$ (e Å^{-3})	2.85	2.2	2.6	

dispersive spectroscopy (EDS) analyzers. For the powder samples, the crystallites were crushed in ethanol, and the small flakes were deposited on a holey carbon film supported by a copper grid. For the characterization of the Ba-based single-crystal structure, the crystal used for the X-ray diffraction refinement was picked and crushed. More than 50 particles of each of the $MV_3P_4O_{17}$ powder samples, M = Ba, Sr, and Pb and the $BaV_3P_4O_{17}$ single crystal, were analyzed.

HREM image simulations were calculated with the Mac-Tempas multislice program.

The magnetic moments were measured with a SQUID magnetometer under a field of 0.3 T after zero field cooling.

Monocrystalline β-$Ba(VO)_3(P_2O_7)_2$. During the crystal growth of $Ba(VO)_3(P_2O_7)_2$, single crystals of a new form were isolated whose structure was revealed to closely be related to that of $K(VO)_3(P_2O_7)_2$ but which were characterized by a different distribution of the P_2O_7 groups.

Crystal Growth. Crystals of the new form were grown in two steps according to the nominal composition "$BaV_3P_4O_{17}$". In a first step $(NH_4)_2HPO_4$ and $BaCO_3$ in the molar ration 4:1 were heated in air at 673 K, in a platinum crucible in order to eliminate CO_2, NH_3, NO_2, and H_2O. In the second step, an adequate amount of VO_2 was added, and the corresponding intimate mixture was heated in an evacuated silica ampule at 1123 K for 20 h. The products were then slowly cooled at 12 K h^{-1} to 413 K and finally quenched to room temperature.

Besides the green polycrystalline powder, a few single crystals were obtained, which were extracted for X-ray diffraction study and microprobe analysis. The cationic composition of those crystals was found to correspond to the formula "BaV_3P_4", in agreement with the structure determination.

Structure Determination. The structural investigation of β-$Ba(VO)_3(P_2O_7)_2$ was performed on one single crystal with dimensions 0.128 × 0.077 × 0.038 mm^3 for the experimental conditions summarized in Table 1. The cell parameters of this new form (Table 1) were found to be similar to those of $K(VO)_3(P_2O_7)_2$.[19] However, the reflection conditions are different, leading to the space group $P11b$ instead of $P2_12_12_1$.

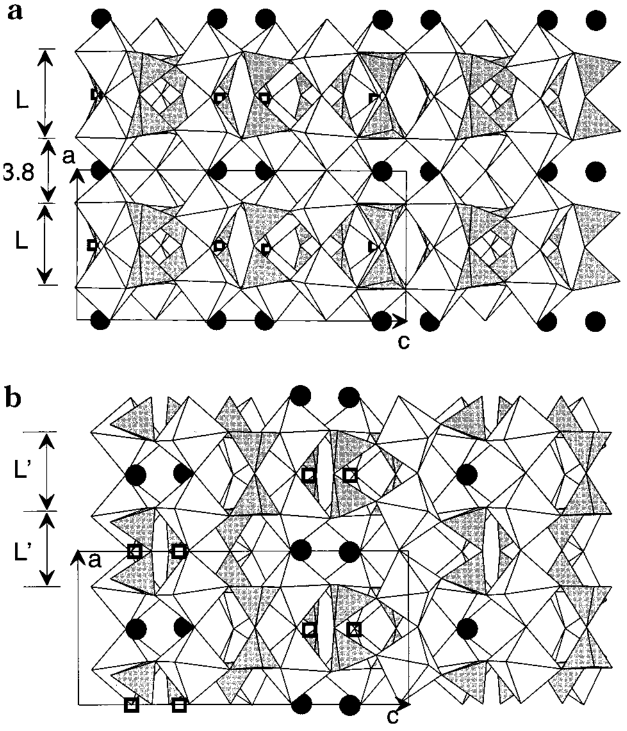

Figure 1. Projection along $\vec{b}$ of (a) the β $Ba(VO)_3(P_2O_7)_2$ and (b) the $K(VO)_3(P_2O_7)_2$ structures. The squares show the empty Ba or K sites.

The structure was solved by the heavy atom method. During the resolution, the difference synthesis evidenced a splitting of some vanadium sites into two half-occupied sites or 20/80% occupied sites with respect to $K(VO)_3(P_2O_7)_2$. The final refinements of the structure led to $R = 0.057$ and $R_W = 0.042$ (Table 1) (The atomic parameters are available in the Supporting Information).

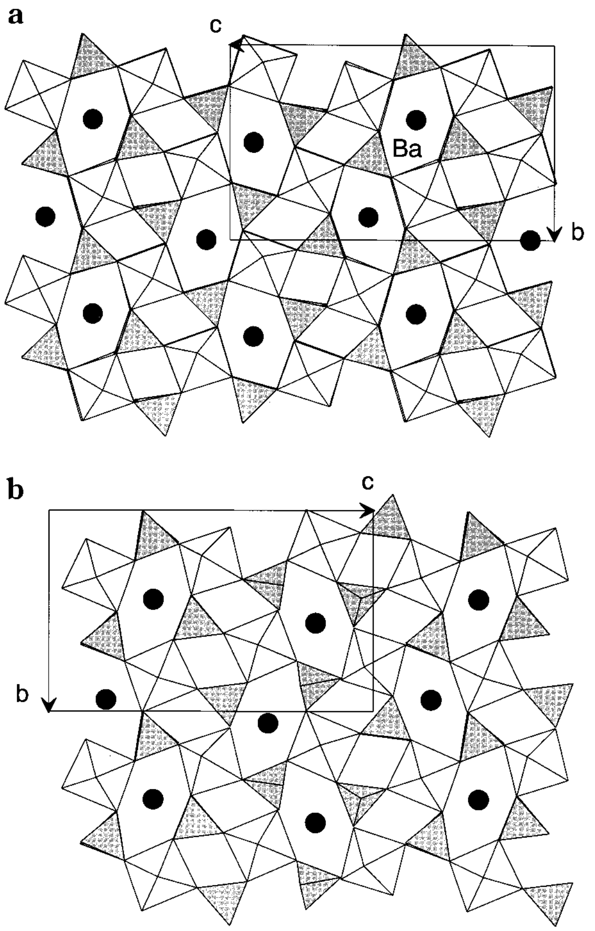

Figure 2. Projection along $\vec{a}$ of (a) the β $Ba(VO)_3(P_2O_7)_2$ and (b) the $K(VO)_3(P_2O_7)_2$ structures, showing the similarities of the two frameworks.

Table 2. Electrostatic Bond Valence Sums for Vanadium in β-$Ba(VO)_3(P_2O_7)_2$, α-$Sr(VO)_3(P_2O_7)_2$, and α-$Pb(VO)_3(P_2O_7)_2$

(a) β-$Ba(VO)_3(P_2O_7)_2$					
V(1)	V(2)	V(3)	V(4)	V(5)	V(6)
4.08	3.98	4.41	4.11	4.15	4.05
(b) α-$Sr(VO)_3(P_2O_7)_2$					
V(1)	V(2)	V(3)			
4.05	4.31	4.23			
(c) α-$Pb(VO)_3(P_2O_7)_2$					
V(1)	V(2)	V(3)			
4.13	4.33	4.17			

Table 3. Cell Parameters Refined from X-ray Powder Diffraction Patterns and Space Group (SG) for the α-$A(V_3O)_3(P_2O_7)_2$ Phases, A = Sr, Pb, and Ba

	a (Å)	*b* (Å)	*c* (Å)	SG
$Sr(VO_3)_3(P_2O_7)_2$	7.6021(3)	10.0715(5)	16.2967(8)	$P2_12_12_1$
$Pb(VO_3)_3(P_2O_7)_2$	7.6092(5)	10.0820(6)	16.3350(10)	$P2_12_12_1$
$Ba(VO_3)_3(P_2O_7)_2$	7.5256(3)	10.0099(5)	16.8475(8)	$P2_12_12_1$

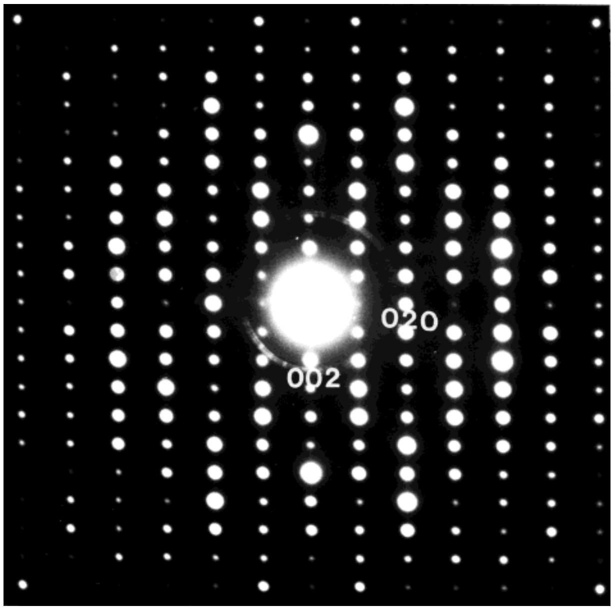

Figure 3. [100] ED patterns, common to the α and β forms.

Description of the Structure. The projection of the structure of β-$Ba(VO)_3(P_2O_7)_2$ along $\vec{b}$ (Figure 1a) shows its close relationships with that of $K(VO)_3(P_2O_7)_2$ (Figure 1b). Both structures consist of ReO_3-type $[VO_3]_\infty$ chains running along $\vec{a}$, interconnected through P_2O_7 groups. The similarity between these two structures is also shown from their projection along $\vec{a}$ (Figure 2), where six-sided tunnels running along $\vec{a}$ can be recognized. In both structures, the relative positions of the octahedral rows and of the tetrahedral rows, and consequently of the tunnels, are similar (Figure 2), but the tilting of the octahedra in β-$Ba(VO)_3(P_2O_7)_2$ (Figure 2a) is different from that in $K(VO)_3(P_2O_7)_2$ (Figure 2b). The difference between the two structures is better understood from their projection along $\vec{b}$ (Figure 1). The distribution of the barium cations and of the P_2O_7 groups in β-$Ba(VO)_3(P_2O_7)_2$ (Figure 2a) is fundamentally different from that in $K(VO)_3(P_2O_7)_2$ (Figure 2b). In both structures, the Ba^{2+} and K^+ cations are located at the level of the apical oxygen of the VO_6 octahedra along $\vec{a}$, forming (100) layers and filling only half of the available A sites. In β-$Ba(VO)_3(P_2O_7)_2$, one A layer out of two is fully occupied by barium (Figure 1a), with the adjacent one being empty, whereas in $K(VO)_3(P_2O_7)_2$, the successive A layers are all half occupied by potassium in an ordered way (Figure 1b). Consequently, two successive Ba layers are spaced by about 7.5 Å, whereas two successive K layers are spaced by about 3.8 Å. The distribution of the P_2O_7 groups is then dictated by this cationic distribution: each time one A site is empty, the three oxygen sites surrounding it, at the same level along $\vec{a}$, are occupied. These anionic sites correspond to the bridging oxygen of the P_2O_7 groups. In other words, three P_2O_7 groups systematically surround one empty A site, and a contrario, the occupation of the A site tends to prevent the location of the P_2O_7 groups around it, likely due to the short A−O distances. Such a behavior is similar to that previously observed for $Ba_3Nb_6Si_4O_{26}$ and the corresponding intergrowths.[22,23] As a consequence, the P_2O_7 groups interconnecting the rows of VO_6 octahedra form fully occupied (100) layers "L" spaced by 3.8 Å in $Ba(VO)_3(P_2O_7)_2$ (Figure 1a), whereas they form half-occupied (100) contiguous layers "L′" in $K(VO)_3(P_2O_7)_2$ (Figure 1b).

The interatomic distances and angles show that the polyhedra are very similar to those observed for $K(VO)_3(P_2O_7)_2$.[19] The geometry of the PO_4 tetrahedra is indeed

---

(22) Choisnet, J.; Nguyen, N.; Groult, D.; Raveau, B. *Mater. Res. Bull.* **1976**, *11*, 887.

(23) Nguyen, N.; Studer, F.; Groult, D.; Choisnet, J.; Raveau, B. *J. Solid State Chem.* **1976**, *19*, 369.

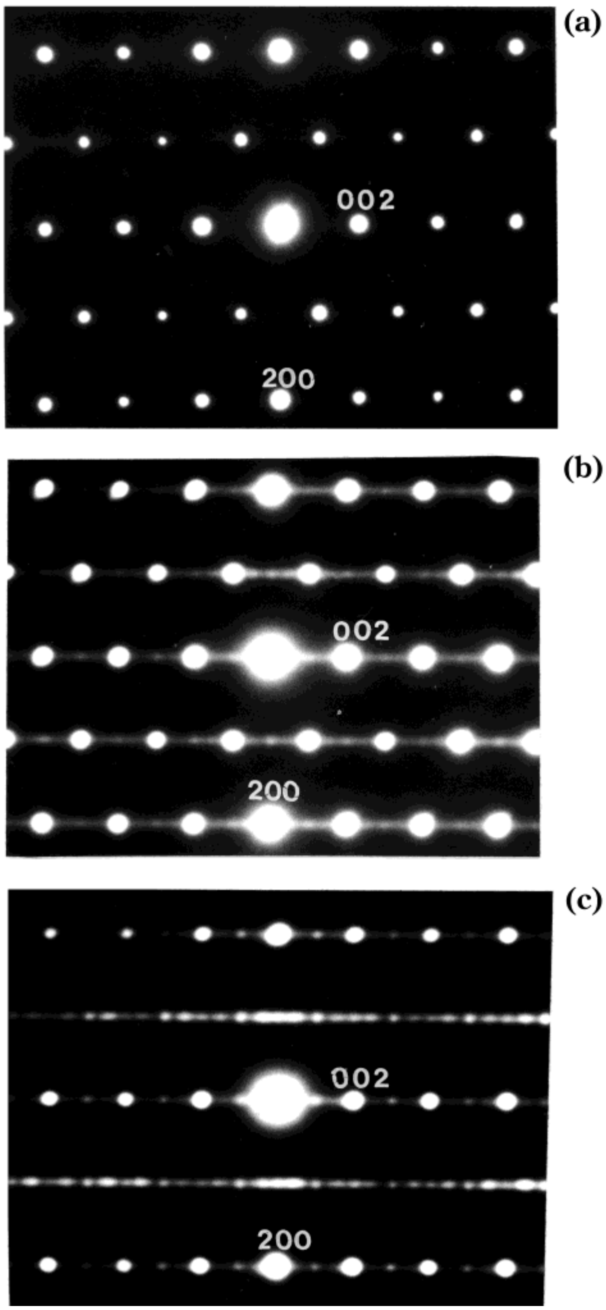

Figure 4. [010] ED patterns observed in the crystalline sample $Ba(VO)_3(P_2O_7)_2$. (a) "Pure" β form, (b) presence of a small amount of the α form, and (c) superimposition of the two systems with extra spots and streaks along *c**, characteristic of stacking faults.

characteristic of the diphosphate groups with one long P−O bond (1.56−1.60 Å) corresponding to the bridging oxygen and three shorter ones (1.49−1.55 Å). The VO_6 octahedra exhibit V−O distances, typically observed for V(IV), with a very short V−O bond (1.61−1.66 Å) opposed to an abnormally long one (2.19−2.32 Å) and four intermediate distances (1.86−2.10 Å). The environment of barium is close to that observed for potassium with nine oxygen atoms as neighbors at distances ranging from 2.73 to 3.15 Å, against 10 oxygen neighbors for potassium at distances ranging from 2.72 to 3.25 Å.

Valency of Vanadium. The evolution of the reciprocal magnetic susceptibility $(\chi - \chi_0)^{-1}$ versus temperature confirms the tetravalent character of vanadium. The slope of the curve in the range 100−350 K leads indeed to a magnetic moment of 1.72 μ_B (μth 1.73).

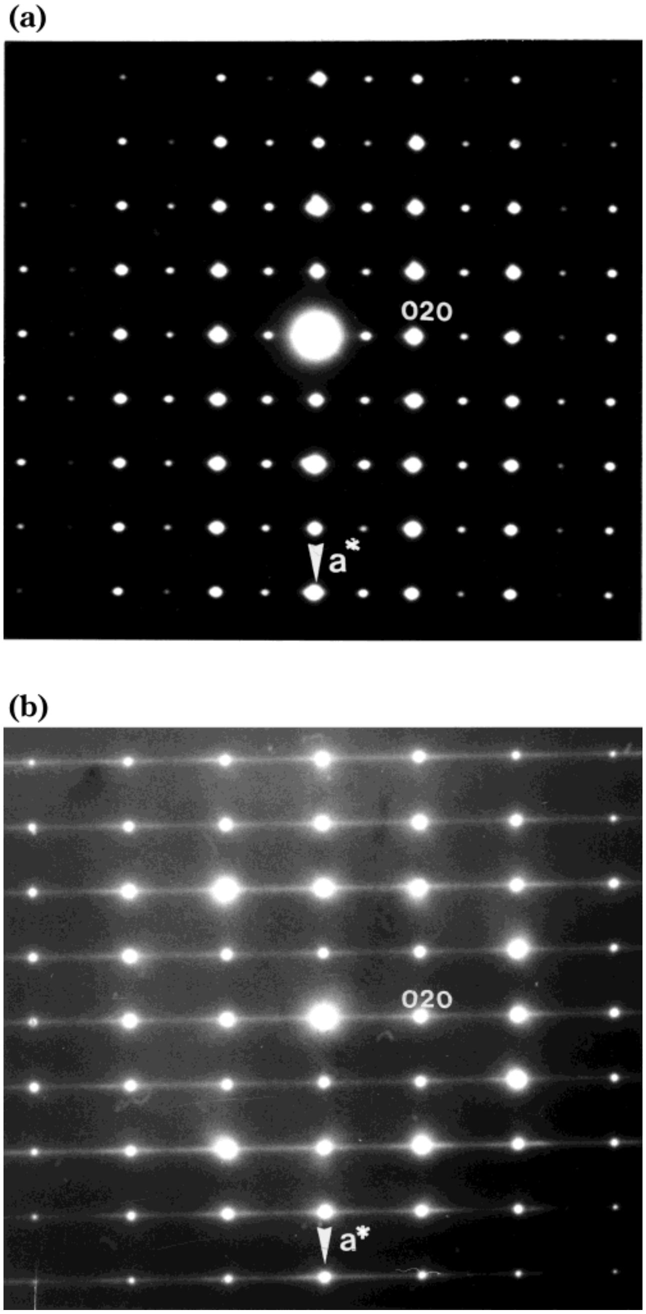

Figure 5. [001] ED patterns: (a) β and (b) α forms with diffuse streaks along *b**.

The calculation of electrostatic valences, based on the Alternatt and Brown model also supports the tetravalence of vanadium (Table 2).

Polycrystalline α-$Ba(VO)_3(P_2O_7)_2$. To understand the different behavior of barium with respect to potassium, chemical synthesis in the form of a polycrystalline sample and its electron microscopy characterization were carried out.

Chemical Synthesis. The synthesis of this phase was also made in two steps. First, a mixture of $Ba(NO_3)_2$, NH_4VO_3, and $(NH_4)_2HPO_4$ in an appropriate ratio according to the final composition $BaV_3P_4O_{17}$ was heated at 673 K for 12 h, to decompose the nitrate, vanadate, and phosphate. Then, the resulting mixture

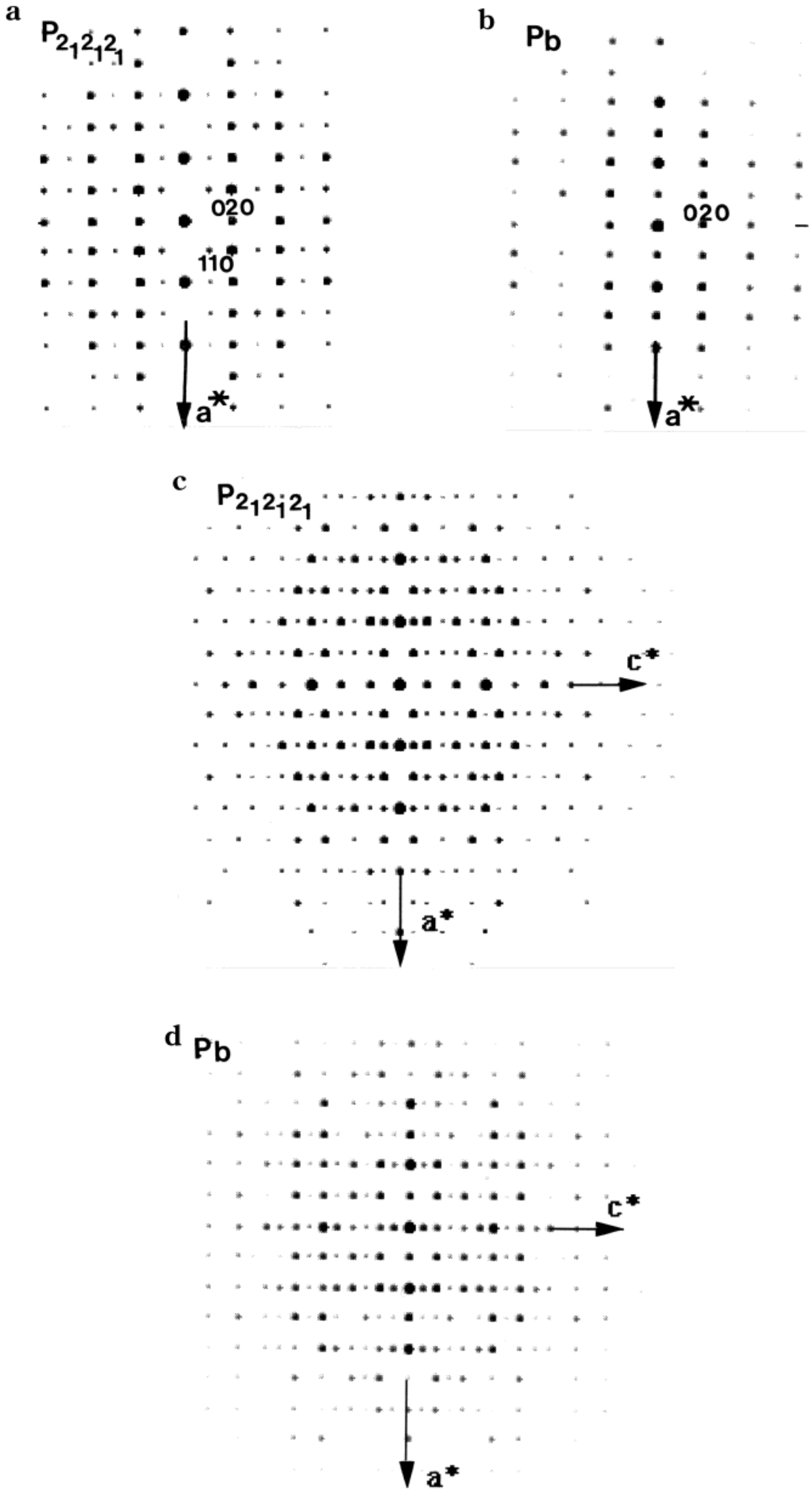

Figure 6. Theoretical [001] ED patterns of the (a) β and (b) α forms and [010] ED patterns of the (c) β and (d) α forms.

was added to the required amount of metallic vanadium (0.6 mol) in order to get the expected compound $BaV_3P_4O_{17}$. The products were heated in an evacuated silica ampule at 1023 K for 12 h and finally quenched to room temperature.

X-ray Powder Diffraction and Electron Diffraction. The XRPD pattern of this polycrystalline phase shows that it can be indexed in an orthorhombic cell with parameters (Table 3) close to those observed from the single-crystal study (Table 1). However, the reflection conditions require a different space group for the indexation. The latter is in fact compatible with the space group $P2_12_12_1$, already observed for $K(VO)_3(P_2O_7)_2$[19], suggesting that this phase corresponds to a second form, called here α-$Ba(VO)_3(P_2O_7)_2$.

The ED patterns of different crystallites show a highly complex microstructure (Figures 3−5) and demonstrate that the two structures β ($P11b$) and α($P2_12_12_1$) coexist

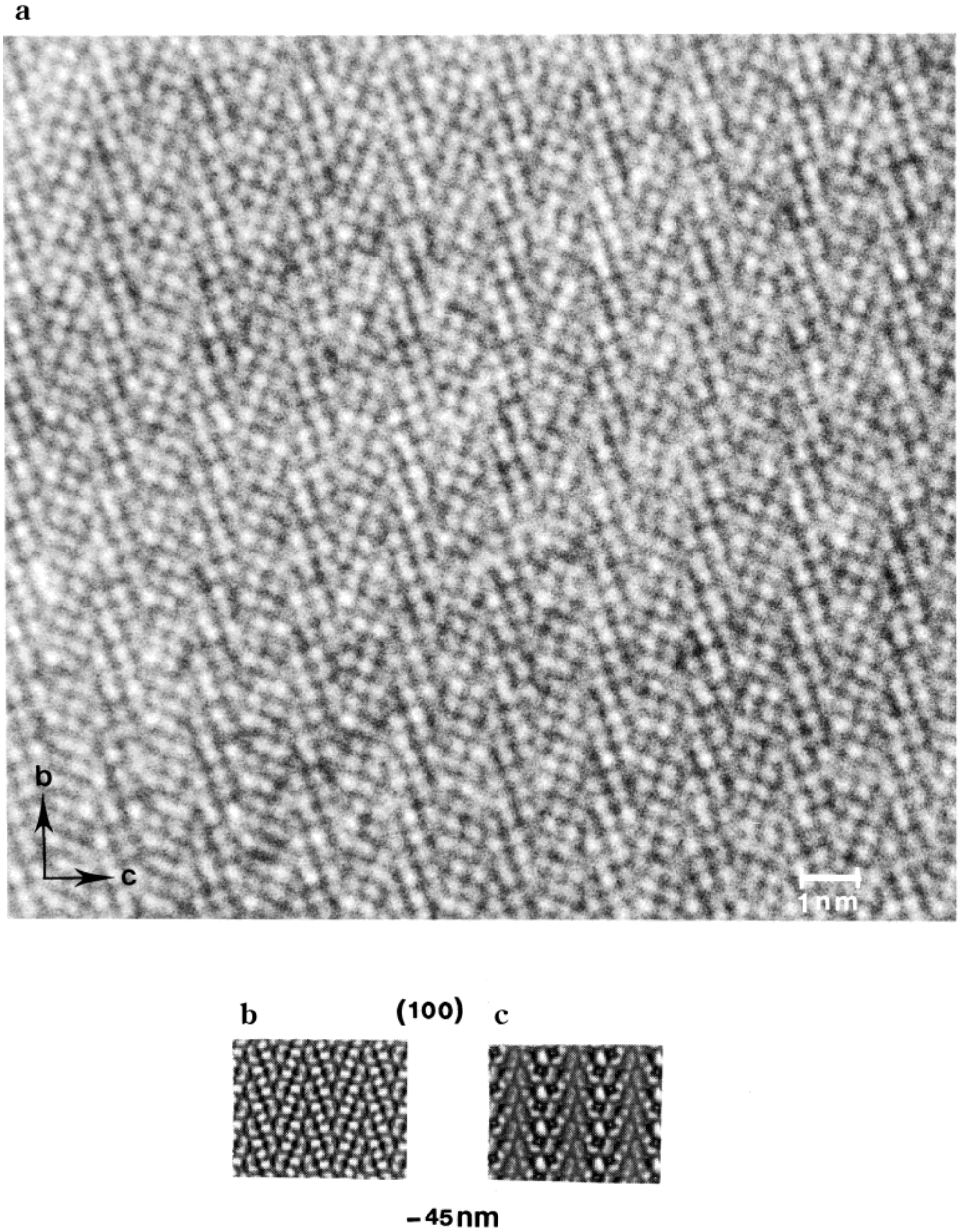

Figure 7. [100] HREM image: (a) experimental $P2_12_12_1$ and $P11b$ models and calculated (b) $P2_12_12_1$ and (c) $P11b$ models.

within most of the crystallites. To understand these observations, theoretical ED patterns of the $P2_12_12_1$ and $P11b$ structures were calculated, using the Mac-Tempas program, which takes into account the double-diffraction phenomena. The four patterns displayed in Figure 6 were calculated for a crystal thickness close to 100 Å. The [100] patterns are common to the two structures, except for the small parameter variations (Figure 3). The [001] patterns (Figure 6a,b) differ by the reflection conditions due to the *b* glide, with $hk0$, $k = 2n$. The [010] patterns are compared in Figure 6c,d; there are no conditions limiting the $h0l$ reflections in either of the structure, but the two structural types clearly differ by the intensities of the reflections, which are "centered" in the first case and not in the second case. The intense reflections of the $P2_12_12_1$ structure obey the *Pmnb* conditions ($h0l$, $h + l = 2n$ and $hk0$, $k = 2n$); this can easily be understood considering the atomic positions, because only the V atoms are displaced from the special positions of the *Pmnb* space group.

Coming back to the experimental ED patterns (Figure 3), it clearly appears that the only orientation which exhibits sharp spots is [100]. By tilting around the a***** axis, diffuse streaks, which are more or less intense depending on the crystallites and crystal areas, are observed in the whole reciprocal space, suggesting a rather high degree of disorder. Three [010] patterns observed in the powder sample, given in Figure 4, illustrate this point. The first one (Figure 4a) is typical of the $P2_12_12_1$ structure with intense centered spots (the uneven $h + l$ reflections are sometimes scarcely visible); in the second one (Figure 4b), weak additional dots characterize the presence of the $P11b$ structure, whereas the third one (Figure 4c) corresponds to the superimposition of the two systems, with extra spots and streaks characteristic of stacking faults. The same effect is observed along [001], as shown from the $P2_12_12_1$ structure-type pattern in Figure 5a and the $P11b$-type structure in Figure 5b. Only a few particles were observed along [010] and [001] without diffuse streaks.

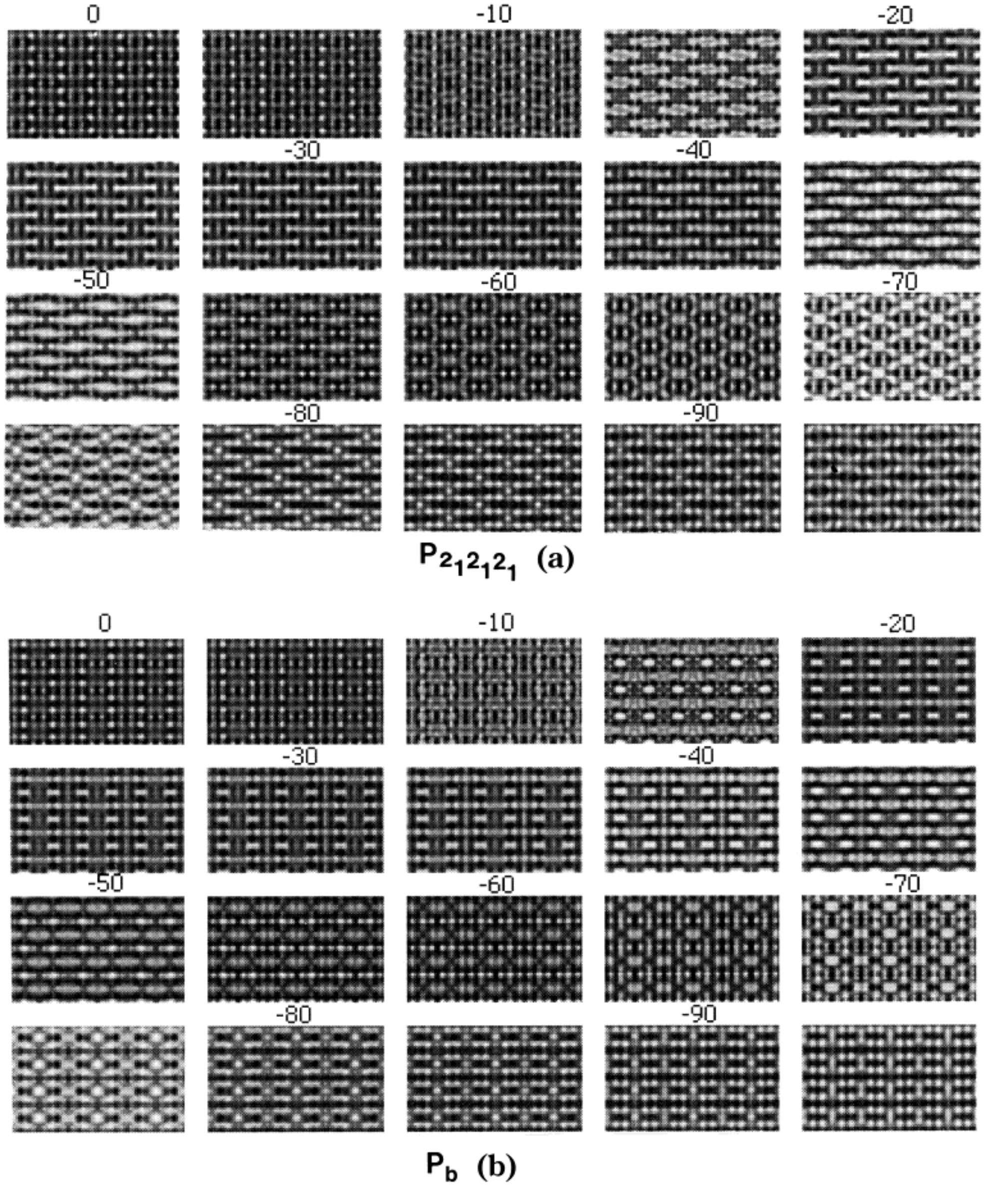

Figure 8. [010] through focus series calculated for a crystal thickness of 20 Å. (a) $P2_12_12_1$ and (b) $P11b$ models (focus values are in nanometers).

These results clearly establish that the $P2_12_12_1$ and the $P11b$ structures coexist, likely as aleatory intergrowths within the same crystal. The diffuse streaks, may also result from a local distortion of the structure due to a partial disordering of the Ba^{2+} cations and consequently of the P_2O_7 groups distribution. The ED study of fragments of the above-studied β-$Ba(VO)_3$-$(P_2O_7)_2$ single-crystal supports this viewpoint. For these fragments, diffuse streaks are still observed, especially along b^*, although they are much less intense. Moreover, areas with the coexistence of the two structural types are seen along [100].

High-Resolution Electron Microscopy (HREM). (1) Regular Areas of the $P2_12_12_1$ Structure. High-resolution images were recorded along the different crystallographic axes. The simulated through focus series were calculated on the basis of the refined parameters obtained from powder sample ($P2_12_12_1$ space group) and single crystal ($P11b$ space group). The contrast strongly evolves with both the focus and the crystal thickness.

The crystallites of the powder samples exhibit very large areas where the experimental contrast fits with the expected one for the $P2_12_12_1$ structure:

A first example of [100] image is given in Figure 7a; it is assumed to be recorded for a focus value close to −45 nm where the bright dots are correlated to the low electron-density zones. The projections of the two structures are in fact very similar along that direction (see Figure 2a,b) so that the variation of contrast will mainly arise from atomic displacements that are not perceptible at a first sight. The theoretical [100] images calculated for the $P2_12_12_1$ and $P11b$ structures (crystal thickness close to 20 Å) are given in parts a and b of Figure 7, respectively. The good fit of the $P2_12_12_1$ model is clearly observed.

A second example is given for the [010] orientation. The two through focus series are compared in Figure 8a and b; they show that it is the best orientation to differentiate the two models, because the barium couples projected in staggered positions in the $P2_12_12_1$ model,

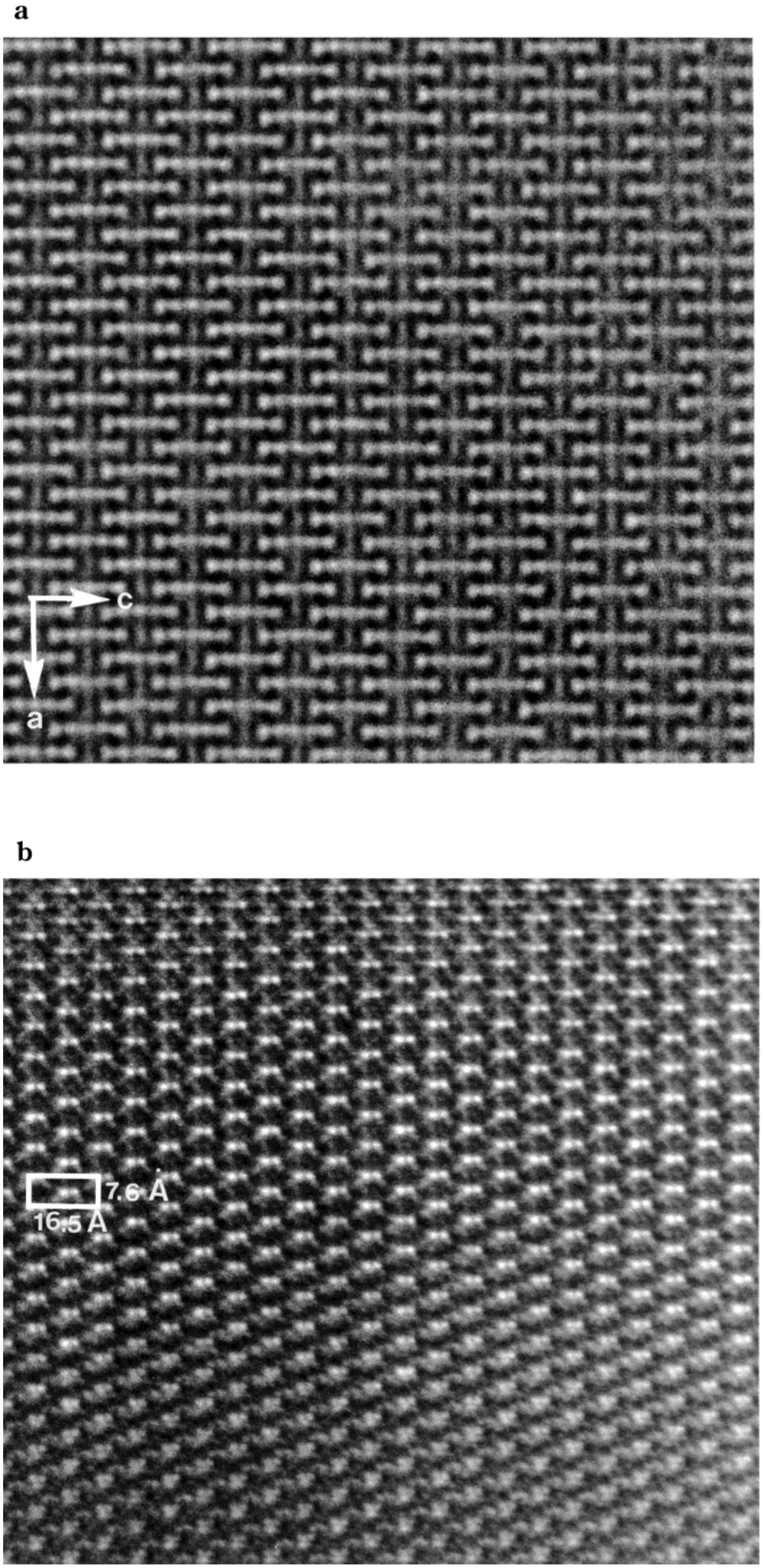

Figure 9. Experimental [010] HREM images for two focus values (a) close to −30 and (b) −60 nm.

whereas they are at the same level and adopt a rectangular arrangement in the *P*11*b* model. The two experimental images in Figure 9a,b are the most characteristic. In Figure 9a, the bright dots are correlated to low electron-density zones (focus value close to the −30 nm), whereas in Figure 9b, the two bright

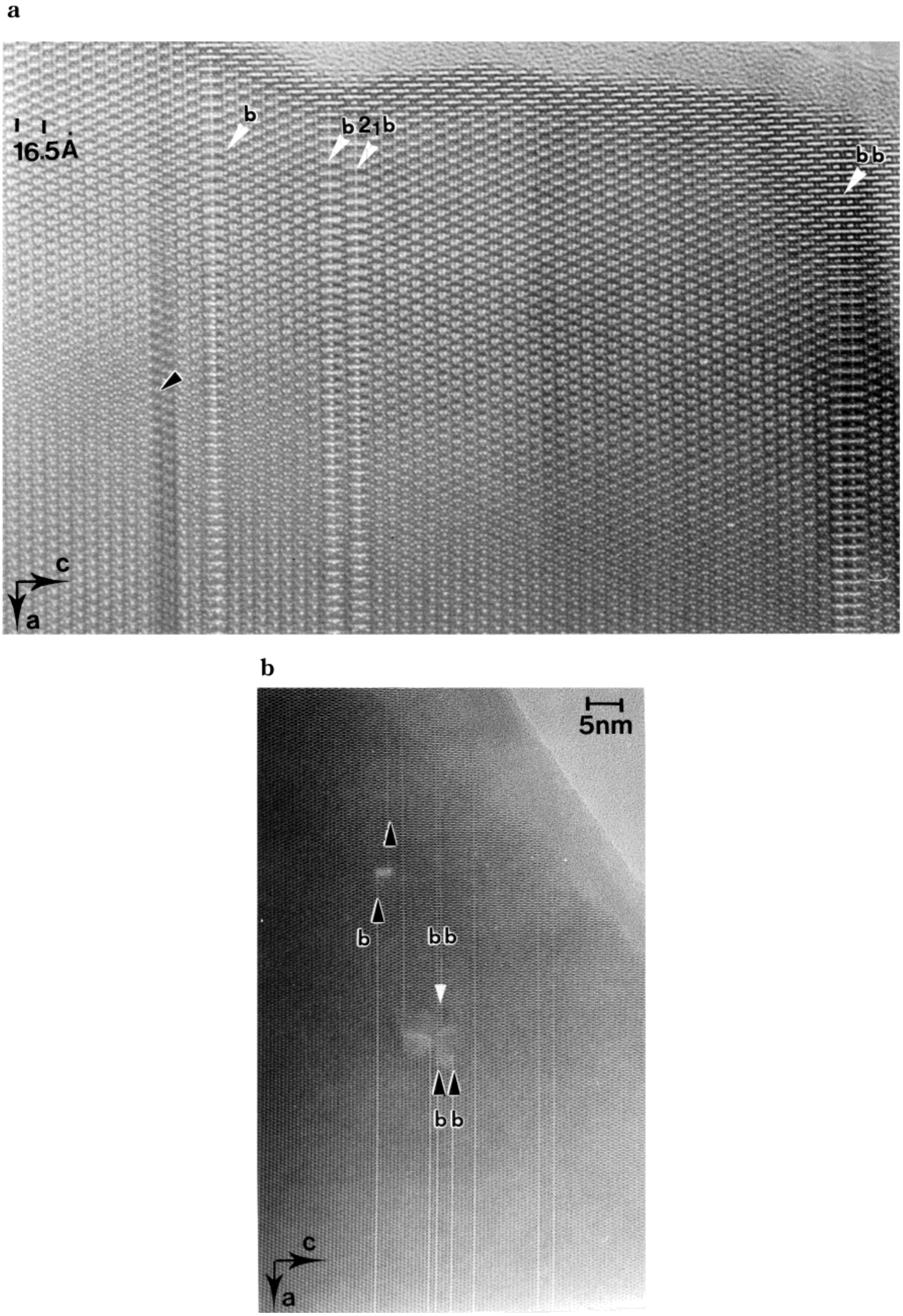

Figure 10. Examples of *P*11*b* defective members in a $P2_12_12_1$ matrix. (a) Linear defects following different sequences and (b) translation of the defects along $\vec{c}$.

dots are correlated to the positions of the couple of Ba (focus value close to −60 nm).

These images show without ambiguity that the average structure of the polycrystalline sample obeys the $P2_12_12_1$ model (Figures 1b and 2b).

(2) *P*11*b*-type Defective Members. The [010] viewing direction allows one to quickly determine the existence of intergrowth defects in the structure. An enlarged image given in Figure 10a shows that there exist two types of intergrowth defect. For the ones that are

indicated by a white arrow, two adjacent Ba couples are no longer in the expected projected staggered positions but at the same level. This means that one *P*11*b*-type slice is locally accommodated within the $P2_12_12_1$ matrix. In this example, three different defective members are observed: a single defective member (denoted *b* in the left part of the image), a double-defective member (denoted *bb* in the right part of the image), and an intergrowth (denoted *b*-2_1-*b)*. The low-resolution image in Figure 10b shows that the defective *b* members can be interrupted or suffer translation along $\vec{c}$, but this always implies strains in the surrounding matrix. The vicinity of the defects are indicated by small arrows; at the level of the translation along $\vec{c}$, a contrast variation is observed (for the present focus value, it correspond to a brighter one).

Coming back to Figure 10a, there are two adjacent slices (indicated by a black arrow) where the contrast is modified, although the staggered positions of the atoms are retained; for the present focus value, the contrast is darker. The image calculations show that this effect is not related to a variation of the occupancy factors of the Ba sites but rather to a local distortion of the structure.

In fact, the observation of numerous crystallites shows that there exist indeed defective *P*11*b*-type members in the $P2_12_12_1$ matrix, but their density is not sufficient enough to involve the intense streaks that are commonly observed in the ED patterns.

(3) Structural Distortions. Viewing the crystallites along [001], the overall images often show large stripes of more or less brightness contrast. One example is given in Figure 11a. The corresponding dark-field images (Figure 11b) confirm that the contrast is not uniform but characteristic of the strain involved by local distortions. The enlarged HREM images (Figure 11c) show that the contrast variation is only observed over a few nanometers and does not exhibit a geometric shape as the defective slices. The focus value of the image is assumed to be close to −95 nm, and the corresponding calculated images are compared for the $P2_12_12_1$ and *P*11*b*-type models. It can be seen that the actual local contrast does not perfectly fit with any of the images but is rather intermediate. This suggests that there exists also another variant of the structure in which the Ba couple would adopt the staggered positions but with a different, likely monoclinic, symmetry. Such an interpretation could explain the rather low density of defective members in the $P2_12_12_1$ structure with regard to the intense streaks, as well as the difficulties for the XRPD refinements.

It would have been interesting to investigate the existence of possible defects in the β-$Ba(VO)_3(P_2O_7)_2$ single crystals. Unfortunately, fragments of these crystals are rapidly amorphised under the electron beam, in contrast to the α-form.

α-$Sr(VO)_3(P_2O_7)_2$ and α-$Pb(VO)_3(P_2O_7)_2$: Single Crystals and Polycrystalline Samples. On the basis of the results obtained for the barium diphosphates, attempts were made to synthesize and grow single crystals of strontium and lead diphosphates.

Synthesis and Crystal Growth. The single growth and quantitative synthesis of polycrystalline samples of the strontium are identical to those described above for the

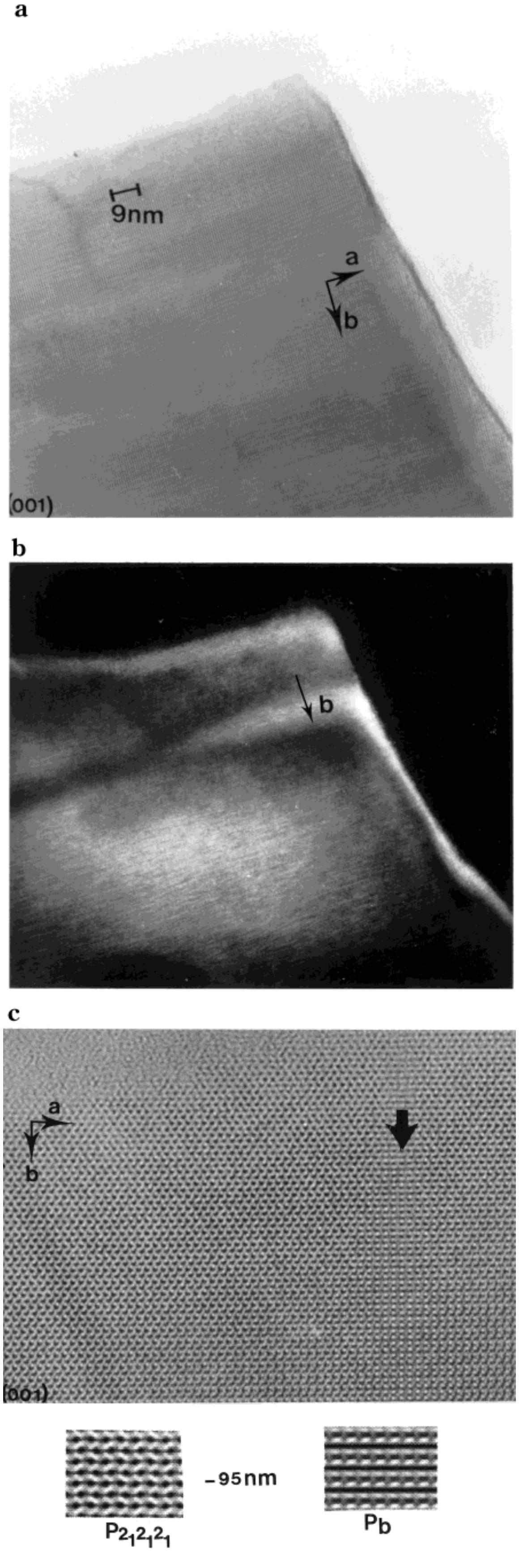

Figure 11. (a) Bright- and (b) dark-field images of crystallites viewed along [001] and (c) enlarged HREM image of a strained crystal. Note the contrast variation at the level of the black arrow. The theoretical images calculated for the $P2_12_12_1$ and *P*11*b* structures are given.

barium diphosphate, $BaCO_3$, and $Ba(NO_3)_2$ being replaced by $SrCO_3$ and $Sr(NO_3)_2$, respectively.

In the case of lead phosphate, the crystal growth was also performed in two steps, but starting with the nominal composition "$PbV_2P_2O_{14}$". In the first step, an adequate mixture of $PbCO_3$ and $(NH_4)_2HPO_4$ was heated at 673 K in a platinum crucible in air for 12 h. Then, the required amount of V_2O_3 was added to the products, and the mixture was heated to 783 K for 12 h, cooled at 12 K h^{-1} to 413 K, and finally quenched to room temperature. In these conditions, besides the green crystals of $PbV_2P_2O_{10}$,[11] blue-green crystals of the new phase were isolated. Their microprobe analysis showed the cationic composition "PbV_3P_4", in agreement with the structure determination.

The quantitative synthesis of the lead phosphate was performed in a manner identical to that for the barium phosphate, but starting from $PbCO_3$ instead of $Ba(NO_3)_2$ and heating the sample up to only 850 K during the second step, instead of 1023 K as for barium.

For the above experimental conditions, both polycrystalline samples $Sr(VO)_3(P_2O_7)_2$ and $Pb(VO)_3(P_2O_7)_2$ are monophasic.

X-ray Diffraction and Electron Microscopy Study. Two single crystals, with dimensions 0.103 × 0.077 × 0.051 and 0.244 × 0.077 × 0.051 mm^3, were selected for Sr and Pb, respectively. Their structure was determined in the same experimental conditions as those described for β-$Ba(VO)_3(P_2O_7)_2$ (Table 1). These compounds exhibit cell parameters similar to those of the barium diphosphate. However, the reflection conditions are different from those of the Ba single crystal, leading to the space group $P2_12_12_1$, already observed for $K(VO)_3(P_2O_7)_2$.[19] Thus, the disphosphates $Sr(VO)_3(P_2O_7)_2$ and $Pb(VO)_3(P_2O_7)_2$ exhibit the α-type structure. Their structure refinement in this space group confirms their isotypism with the potassium diphosphate, leading to reliability factors $R = 0.04$ and $R_W = 0.037$ for Sr and $R = 0.026$ and $R_W = 0.023$ for Pb (Table 1) (The atomic coordinates are available in the Supporting Information). The configuration of the $[VO_3]_\infty$ chains suggests the possibility of enanthiomorphic configurations. The latter was tested by changing the sign of the *x* coordinates of the atoms. It clearly appears that the potassium and strontium diphosphate structures are superimposable, whereas the lead diphosphate exhibits the enanthiomorphic configuration.

The electron diffraction study of these compounds confirms that the matrix exhibits $P2_12_12_1$ symmetry. Only weak streaks are observed for Sr, suggesting a low degree of disorder. A second type of symmetry, $P112/n$, is observed for a few Pb-based crystallites, which suggests the possibility of a different distribution of lead cations and P_2O_7 groups.

The interatomic distances and angles show a geometry of the different polyhedra similar to that observed for α- and β-$Ba(VO)_3(P_2O_7)_2$. The PO_4 tetrahedra exhibit indeed a longer P−O bond (1.560−1.592 Å), characteristic of the bridging oxygen of the P_2O_7 groups, and three shorter ones (1.478−1.534 Å). Similarly the VO6 octahedra are characterized by a shorter V═O bonds (1.591−1.629 Å) opposed to a long one (2.194−2.330) and four intermediate V−O bonds (1.930−2.066 Å). The Sr^{2+} and Pb^{2+} cations have the same environment as K^+ in $K(VO)_3(P_2O_7)_2$ with distances ranging from 2.57 to 3.27 Å, and from 2.58 to 3.22 Å, respectively.

Magnetic susceptibility measurements lead to a magnetic moment of 1.68 μ_B and 1.59 μ_B for Sr and Pb phases, respectively, in agreement with the theoretical value of 1.73 μ_B for tetravalent vanadium. The tetravalence of vanadium is confirmed by electrostatic valence calculations (Table 2).

Concluding Remarks

This study demonstrates the great ability of diphosphate groups to tune vanadium octahedra, leading to a complex chemistry characterized by various possible distributions of the diphosphate groups in closely related structures, so that intergrowth phenomena are observed. Such a great flexibility of the V−P−O framework is to be compared to the phosphate tungsten bronze family. It suggests that many other vanadophosphates, with a complex chemistry should be generated in the future, especially in the vanadium-rich region, with a view of developing new physical properties.

Supporting Information Available: Tables of atomic positional, isotropic displacement, site occupancy parameters, distances, and angles in β-$Ba(VO)_3(P_2O_7)_2$ and α-$Sr(VO)_3(P_2O_7)_2$ and tables of atomic positional, isotropic displacement, and site occupancy parameters in α-$Pb(VO)_3(P_2O_7)_2$. This material is available free of charge via the Internet at http://pubs.acs.org.

CM9904842